PAPER

Check for updates

Fluoroborate ionic liquids as sodium battery electrolytes†

Dale T. Duncan,[a] Samantha L. Piper, [ID][a] Maria Forsyth,[b] Douglas R. MacFarlane [ID][a] and Mega Kar [ID] *[b]

High-voltage sodium batteries are an appealing solution for economical energy storage applications. Currently available electrolyte materials have seen limited success in such applications therefore the identification of high-performing and safer alternatives is urgently required. Herein we synthesise six novel ionic liquids derived from two fluoroborate anions which have shown great promise in recent battery literature. This study reports for the first time the electrochemically applicable room-temperature ionic liquid (RTIL) N-ethyl-N,N,N-tris(2-(2-methoxyethoxy)ethyl)ammonium (tetrakis)hexafluoroisopropoxy borate ($[N_{2(2O2O1)3}][B(hfip)_4]$). The RTIL shows promising physical properties with a very low glass-transition at -73 °C and low viscosity. The RTIL exhibits an electrochemical window of 5.3 V on a glassy carbon substrate which enables high stability electrochemical cycling of sodium in a 3-electrode system. Of particular note is the strong passivation behaviour of $[N_{2(2O2O1)3}][B(hfip)_4]$ on aluminium current-collector foil at potentials as high as 7 V (*vs.* Na$^+$/Na) which is further improved with the addition of 50 mol% Na[FSI]. This study shows $[B(hfip)_4]^-$ ionic liquids have the desired physical and electrochemical properties for high-voltage sodium electrolytes.

Introduction

Rechargeable batteries as energy storage systems have become fully integrated into many facets of modern life. Batteries provide a highly convenient energy storage solution for many applications, but their current design does not provide a sufficient safety profile, as indicated by ongoing reports of lithium-ion battery (LIB) fires.[1] These fires are difficult to extinguish and produce significant quantities of toxic vapour; they have occurred in electric vehicles, mobile phones and both residential and grid-scale battery stacks.[2-6] Ionic liquids (ILs) have negligible vapour pressure and low flammability which provides a safer alternative to conventional organic electrolytes (*e.g.* 1 M NaPF$_6$ in ethylene carbonate (EC) and dimethyl carbonate (DMC)) which are often flammable and produce harmful species such as PF$_5$ and HF upon combustion.[7,8] The low volatility also impedes thermal runaway which greatly improves the safety of the electrolyte and of the overall device compared to organic electrolytes.[9-11] The benefits of ILs expand beyond safety, also offering higher thermal stability,[12] wider

electrochemical windows[13] and structural tunability. As such, ILs are shown to be viable electrolyte matrices in LIB and beyond-LIB technologies including sodium-ion, sodium–metal and high voltage lithium–metal batteries.[14-19]

ILs are low melting point salts and have shown promise for a variety of applications beyond batteries including as sensors, lubricants, corrosion-inhibitors, recycling and separation processes.[20] The material bulk properties are heavily influenced by the choice of cation and anion, and are a reflection of intermolecular interactions between the ions: weak and labile interactions are preferred which is reflected in high conductivity and fluidity of the bulk material. Anions offering weak and labile ion–ion interactions support high ionicity and are classified as weakly-coordinating anions (WCAs), often due to their charge-diffuse structure.[21-23] Two common WCAs are hexafluorophosphate and bis(fluorosulfonyl)imide ($[PF_6]^-$ and $[FSI]^-$, respectively) of which $[PF_6]^-$ is of great importance to LIBs as a component of the standard LP30 (1.0 M Li$[PF_6]$/EC:DMC, 1:1 vol) electrolyte. The anion $[FSI]^-$ has lower symmetry and greater charge-delocalisation than $[PF_6]^-$ and therefore exhibits weaker ion–ion interactions and better physical properties than $[PF_6]^-$.[24,25] WCAs are particularly appealing for electrochemical applications as electrolytes offering high conductivity and fluidity in addition to high cathodic stability of the anion.

Identification of alternative WCAs is of research interest as currently available anions have significant drawbacks, such as

[a] *School of Chemistry, Monash University, Wellington Road, Clayton, VIC 3800, Australia*

[b] *Institute of Frontier Materials, Deakin University, 221 Burwood Highway, Burwood, VIC 3125, Australia. E-mail: m.kar@deakin.edu.au*

27718 | *Phys. Chem. Chem. Phys.*, 2023, **25**, 27718–27730

This journal is © the Owner Societies 2023

the oxidative corrosion of [FSI]$^-$ towards aluminium in conventional electrolytes and the atmospheric instability of [PF$_6$]$^-$. Boron-containing anions such as tetrafluoroborate, difluoro-(oxalato)borate and *mono*-closoborane ([BF$_4$]$^-$, [DFOB]$^-$ and [*closo*-CB$_{11}$H$_{12}$]$^-$, respectively) are shown to be comparatively stable at high potentials and in air. Preliminary research with NaBF$_4$ identified the salt to be an attractive material for non-flammable ionic liquid electrolytes, however it possesses limited solubility in ionic liquids which was addressed with a polyether solvent;[26] the salt is also susceptible to hydrolysis. [DFOB]$^-$ has improved atmospheric stability and generates fewer hazardous decomposition products upon exposure to air when compared to [BF$_4$]$^-$.[27] The anion also shows high oxidative stability against stainless steel with an initial decomposition potential of 5.8 V *vs.* Na$^+$/Na with 1 M NaDFOB/EC:DEC 1:1 vol.[28] The boron cluster [*closo*-CB$_{11}$H$_{12}$]$^-$ has also been shown to be useful as an ionic liquid anion with alkoxy-ammonium cations [N$_{2(2O2O1)3}$]$^+$ and [N$_{4(2O2O1)3}$]$^+$ exhibiting an electrochemical window of 4.55 V and low glass-transition (T_g) of −52 and −47 °C, respectively.[29]

The fluoroborate salts, sodium (tetrakis)hexafluoroisopropoxy borate (Na[B(hfip)$_4$]·xDME, where DME = 1,2-dimethoxyethane) and sodium (tetrakis)trifluoroethoxy borate (Na[B(tfe)$_4$]), were first reported in 2011 and 2014 respectively,[30,31] however their use as battery electrolytes in organic solvents was only recently realised.[32–34] From our recent publication, an electrolyte comprised of 0.5 M Na[B(hfip)$_4$] in DME demonstrated stable electrochemical cycling over 300 cycles at 0.1 mA cm^{-2} in a Na‖Na symmetrical cell with very low overpotentials, below 2 mV.[34] This impressive electrochemical performance was attributed to the weakly coordinating nature of [B(hfip)]$^-$ which results in high ion-dissociation of Na$^+$. Moreover, the anion shows superior cathodic stability against aluminium, evenly passivating the surface with AlF$_3$ and NaF.[34]

In other work, Roy *et al.* has shown 0.5 M Li[B(hfip)$_4$]·3DME in EC:DMC (1:1 vol) to be an effective electrolyte in high-voltage Li–metal full-cells, as well as demonstrating exceptional atmospheric stability.[32] Li[B(hfip)$_4$]·3DME exposed to air for 24 hrs showed no deterioration of electrochemical performance in a full-cell when compared to an equivalent electrolyte with nonexposed salt. The promising outcomes of these studies have prompted further studies with [B(hfip)$_4$]$^-$, however the use of flammable organic solvents in these electrolytes has raised concerns regarding safety and high voltage stability.[35] We seek to eliminate the use of such solvents by utilising the fluoroborates anions in ionic liquids. To date no electrochemically applicable ILs with [B(tfe)$_4$]$^-$ or [B(hfip)$_4$]$^-$ have been reported.

Anion and cation structures forming the basis of this work are shown in Fig. 1. Three cations are studied with the borate anions; *N*-ethyl-*N,N,N*-tris(2-(2-methoxyethoxy)ethyl)ammonium (**1**), iso-butyl(diethyl)methyl phosphonium (**2**) and *N*-methyl-*N*-propylpyrrolidinium ([N$_{2(2O2O1)3}$]$^+$, [P$_{122i4}$]$^+$ and [C$_3$mpyr]$^+$, respectively) which are of different chemical classes (ammonium, phosphonium and pyrrolidinium, respectively) and chosen based on literature merit for new electrolyte materials.[29,36,37] The electrochemical stability and low T_g of [N$_{2(2O2O1)3}$]$^+$ ILs are appealing and will likely improve the physical and electrochemical properties of fluoroborate products.[29,38] ILs with [P$_{122i4}$]$^+$ often display organic ionic plastic crystal (OIPC) behaviour such as [P$_{122i4}$][DFOB] which exhibits this behaviour beyond −13 °C;[37] the similar [P$_{111i4}$]$^+$ ILs also exhibit excellent physical and electrochemical properties.[39] ILs with [C$_3$mpyr]$^+$ are well established in literature and have been used in SIB and Li–metal batteries.[14,17,40]

In this study the novel fluoroborate ionic liquids and organic salts have been prepared and screened for useful phase behaviour as well as determination of the thermal stability and flammability hazard of the ILs. Two RTILs are identified and physically characterised against related materials to understand the effect of the charge-diffuse fluoroborate anion. The novel IL [N$_{2(2O2O1)3}$][B(hfip)$_4$] is further studied to determine its electrochemical stability, applicability to Na-electrochemistry *via* 3-electrode cyclic voltammetry and a thorough investigation into the underlying reason for the high voltage Al passivation behaviour *via* comprehensive surface analysis. [N$_{2(2O2O1)3}$]-[B(hfip)$_4$] is identified as a promising candidate for future research in SIB applications with the RTIL showing very high fluidity, high solubility of Na[FSI], high electrochemical cycling stability in a 3-electrode cell across 15 cycles and cathodic passivation of aluminium up to 7 V *vs.* Na$^+$/Na. The high voltage
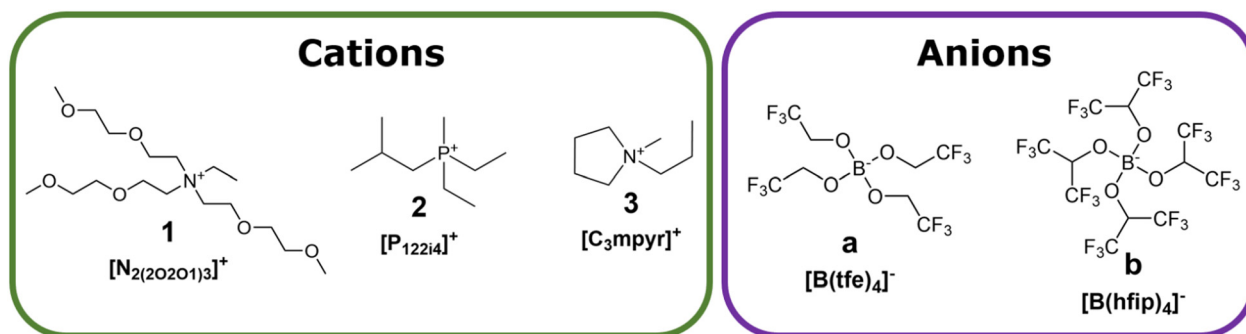

Fig. 1 Chemical structures and abbreviations of the cations *N*-ethyl-*N,N,N*-tris(2-(2-methoxyethoxy)ethyl)ammonium [N$_{2(2O2O1)3}$]$^+$ (**1**), iso-butyl(diethyl)methyl phosphonium [P$_{122i4}$]$^+$ (**2**) and *N*-methyl-*N*-propylpyrrolidinium [C$_3$mpyr]$^+$ (**3**), and anions (tetrakis)trifluoroethoxy borate [B(tfe)$_4$]$^-$ (a) and (tetrakis)hexafluoroisopropoxy borate [B(hfip)$_4$]$^-$ (b).

This journal is © the Owner Societies 2023

Phys. Chem. Chem. Phys., 2023, **25**, 27718–27730 | **27719**

passivation of Al of neat $[N_{2(2O2O1)3}][B(hfip)_4]$ was further improved with the addition of 50 mol% Na[FSI], resulting in a surface with smooth morphology derived from $[FSI]^-$.

Experimental

Synthetic procedures

All reagents were used as received. $Na[B(OCH_2CF_3)_4]$ $(Na[B(tfe)_4])$, $Li[B(OCH(CF_3)_2)_4]\cdot x$DME $(Li[B(hfip)_4]\cdot 3DME)$ and $N_{2(2O2O1)3}$Br were synthesised according to published methods.[29,32,34]

Synthesis of $[N_{2(2O2O1)3}][B(tfe)_4]$ (1a). $[N_{2(2O2O1)3}]$Br and $Na[B(tfe)_4]$ (1.00:1.01 molar ratio) were mixed in 50 mL acetonitrile (MeCN). The mixture was stirred overnight under N_2. The solvent was removed by rotovap and minimal dichloromethane (DCM) was added to dissolve the crude product, then filtered with a 0.2 μm PTFE syringe filter (25 mm $\varnothing$). The DCM was collected and centrifuged at 8000 rpm for 10 minutes. The liquid phase was collected and the sediment was discarded. The collected liquid was concentrated by rotovap and the product dried further until 8.0×10^{-3} mbar vacuum was held for two to four hours. ^{1}H NMR: δ 3.83–3.77 ppm, 6H, t; δ 3.71–3.63 ppm, 8H, q; δ 3.63–3.58 ppm, 6H, t; δ 3.58–3.53 ppm, 6H, t; δ 3.53–3.46 ppm, 2H, q; δ 3.46–3.41 ppm, 6H, m; δ 3.26 ppm, 9H, s; δ 1.25–1.18 ppm, 3H, t. ^{11}B NMR: 2.24, 1B, m. ^{19}F NMR: −74.3 ppm, 12F, s.

Synthesis of $[P_{122i4}][B(tfe)_4]$ (2a). $[P_{122i4}][TOS]$ (where TOS = $[H_3C(C_6H_4)SO_3]^-$) and $Na[B(tfe)_4]$ (1.00:1.01 molar ratio) were mixed in 50 mL MeCN. The mixture was stirred overnight under N_2. The solvent was removed by rotovap and minimal DCM was added to dissolve the crude product, then filtered with a 0.2 μm PFTE syringe filter (25 mm $\varnothing$). The DCM was collected and centrifuged at 8000 rpm for 10 minutes. The liquid phase was collected and the sediment was discarded. The clear liquid was then concentrated by rotovap and the product dried further until 8.0×10^{-3} mbar vacuum was held for two to four hours. ^{1}H NMR: δ 3.73–3.61 ppm, 8H, q; δ 2.53–2.49 ppm, 2H, m; δ 2.26–2.11 ppm, 2H, m; δ 2.09–1.96 ppm, 1H, m; δ 1.85–1.79 ppm, 3H, d; δ 1.20–1.09 ppm, 6H, m; δ 1.05–1.01 ppm, 6H, d. ^{11}B NMR: δ 2.27 ppm, 1B, s. ^{19}F NMR: δ −74.27 ppm, 12F, s.

Synthesis of $[C_3mpyr][B(tfe)_4]$ (3a). $[C_3mpyr]$Br and $Na[B(tfe)_4]$ (1.00:1.01 molar ratio) were mixed in 50 mL MeCN. The mixture is stirred overnight under N_2. The solvent was removed by rotovap and minimal DCM was added to dissolve the crude product, then filtered with a 0.2 μm PFTE syringe filter (25 mm $\varnothing$). The DCM was collected and centrifuged at 8000 rpm for 10 minutes. The liquid phase was collected and the sediment was discarded. The collected liquid was concentrated by rotovap and the product dried further until 8.0×10^{-3} mbar vacuum was held for two to four hours. ^{1}H NMR: δ 3.88–3.74 ppm, 8H, q; δ 3.53–3.37 ppm, 2H, m; δ 3.30–3.22 ppm, 4H, m; δ 2.98 ppm, 3H, s; δ 2.14–2.02 ppm, 4H, m; δ 1.78–1.65 ppm, 2H, m; δ 0.95–0.86 ppm, 3H, t. ^{11}B NMR: δ 2.23 ppm. ^{19}F NMR: δ −74.3 ppm.

Synthesis of $[N_{2(2O2O1)3}][B(hfip)_4]$ (1b). $[N_{2(2O2O1)3}][Br]$ and $Li[B(hfip)_4]\cdot 3DME$ (1.00:1.02 molar ratio) precursors were placed in a flask with 50 mL DCM. The mixture was stirred overnight under N_2. The mixture was filtered and an aqueous/DCM biphasic extraction was performed 5 times on the DCM phase to remove residual Li biproduct and reactant. The DCM phase was concentrated by rotovap and the product dried further until 8.0×10^{-3} mbar vacuum was held for two to four hours. ^{1}H NMR: δ 4.65 ppm, 4H, s; δ 3.84–3.77 ppm, 6H, t; δ 3.65–3.59 ppm, 6H, t; δ 3.59–3.54 ppm, 6H, m; δ 3.52–3.49 ppm, 2H, m; δ 3.49–3.43 ppm, 6H, m; δ 3.27 ppm, 9H, s; δ 1.28–1.23 ppm, 3H, t. ^{11}B NMR: 1.63, 1B, m. ^{19}F NMR: −74.6 ppm, 24F, s. MS $[ES]^+ = 352.28$, $[ES]^- = 678.99$.

Synthesis of $[P_{122i4}][B(hfip)_4]$ (2b). $[P_{122i4}][TOS]$ (where TOS = $[H_3C(C_6H_4)SO_3]^-$) and $Li[B(hfip)_4]\cdot 3DME$ (1.00:1.02 molar ratio) precursors were placed in a flask with 50 mL DCM. The mixture was stirred overnight under N_2. The mixture was filtered and an aqueous/DCM biphasic extraction was performed 5 times on the DCM phase to remove residual Li biproduct and reactant. The DCM phase was concentrated by rotovap and the product dried further until 8.0×10^{-3} mbar vacuum was held for two to four hours. ^{1}H NMR: δ 4.65 ppm, 4H, s; δ 2.53–2.49 ppm, 2H, m; δ 2.26–2.12 ppm, 2H, m; δ 2.09–1.95 ppm, 1H, m; δ 1.84–1.80 ppm, 3H, d; δ 1.19–1.09 ppm, 6H, m; δ 1.05–1.01 ppm, 6H, d. ^{11}B NMR: 1.62, 1B, m. ^{19}F NMR: −74.6 ppm, 24F, s. MS $[ES]^+ = 161.15$, $[ES]^- = 678.97$.

Synthesis of $[C_3mpyr][B(hfip)_4]$ (3b). $[C_3mpyr][Br]$ and $Li[B(hfip)_4]\cdot 3DME$ (1.00:1.02 molar ratio) precursors were placed in a flask with 50 mL DCM. The mixture was stirred overnight under N_2. The mixture was filtered and an aqueous/DCM biphasic extraction was performed 5 times on the DCM phase to remove residual Li biproduct and reactant. The DCM phase was concentrated by rotovap and the product dried further until 8.0×10^{-3} mbar vacuum was held for two to four hours. ^{1}H NMR: δ 4.65 ppm, 4H, s; δ 3.51–3.37 ppm, 2H, m; δ 3.28–3.22 ppm, 4H, m; δ 2.98 ppm, 3H, s; δ 2.10–2.05 ppm, 4H, m; δ 1.78–1.65 ppm, 2H, m; δ 0.96–0.89 ppm, 3H, t. ^{11}B NMR: 1.62, 1B, m. ^{19}F NMR: −74.6 ppm, 24F, s. MS $[ES]^+ = 128.11$, $[ES]^- = 678.99$.

Crystal structure and refinement

Single crystal X-ray crystallographic data was collected on a Rigaku Xtalab Synergy Dualflex using a monochromator equipped with Cu-Kα (λ = 1.5418 Å) radiation, at 123 K. Data was processed using proprietary software CrysAlisPro.[41] The structures were solved and refined using the SHELX software suite[42,43] and refined against F^2 using Olex2[44] as a graphical interface. Non-hydrogen atoms were refined with anisotropic displacement parameters. Alkyl hydrogen atoms were included in calculated positions (riding model).

Thermal properties

Phase transition temperatures (melting T_m, solid–solid T_{ss}) and enthalpies were determined using a DSC TA Q200 calorimeter (TA Instruments). The equipment was calibrated using standard indium (TA Instruments, T_m = 156.6 °C, ΔH_f = 28.47 J g^{-1}) and cyclohexane (Sigma-Aldrich, T_m = 8 °C). Measurements were performed under a N_2 atmosphere with a sample size of

3–5 mg and a scanning rate of 10 °C min^{-1}. Presented values were taken from the second heating cycle unless otherwise specified. T_m was considered as the peak maximum and ΔH_f as the area of the peak.

Thermal stability was determined by thermogravimetric analysis (TGA) using Mettler Toledo TGA/DSC 1 STARe system. Samples were heated with a dynamic heating rate of 10 °C min^{-1} over 40 to 450 °C under N_2. Material flammability was determined by igniting approximately 0.25 g or 0.25 mL of IL on Al-foil with a butane torch. The sample was exposed to the flame for 2 seconds to ensure combustion of the sample; the material was deemed flammable if combustion was sustained for one second or more following removal of the ignition source.

Physical properties

Density and viscosity measurements were conducted in 5 °C increments from 20 to 90 °C. For density measurements, 1.8 mL electrolyte was injected into a Mettler Toledo DM40 density meter. For viscosity measurements, a 1.59 mm $\varnothing$ steel rolling-ball capillary tube was prepared and inserted into an Anton Paar Lovis 2000ME viscosity meter at 30° incline. Conductivity measurements for liquid samples were conducted with electrical impedance spectroscopy (EIS) on a Biologic MTZ-35 instrument with an air-tight dip-cell fitted with Pt electrodes, designed in-house. For solid-state conductivity, pellets (13 mm $\varnothing$) were prepared with a hydraulic press to yield pellets of 0.5 to 0.8 mm thickness. The pellets were analysed in a barrel cell with stainless-steel electrode, the reported value is the average of two measurements. The frequency range of analysis was 7.0×10^7 to 1 Hz, with 10 points per decade and 10 cycles per measurement. Instrument temperature was controlled by a Eurotherm 2204e thermostat with analysis in 5 °C increments from 25 °C to 90 °C. The conductivity of the electrolytes was determined by relating the touch-down point of the Nyquist Plot against a 0.01 M KCl/H_2O.

Electrochemical characterisation

All electrolytes were stored and prepared in an Ar glovebox (<0.1 ppm H_2O, <0.1 ppm O_2). The Na[FSI]:**1b** electrolyte was prepared by measuring equimolar quantities before dissolution at 50 °C with stirring over 48 hours.

Three-electrode cells were prepared with 0.5 mL electrolyte. The electrochemical window was determined with a glassy carbon working electrode and Pt wires as the counter electrode and pseudo reference electrode; the cell was referenced to the Fc$^+$/Fc redox. The oxidative and reductive stability were determined independently with a clean cell and electrodes. The cells were cycled in a cyclic voltammetry protocol at 25 mV s^{-1} from open-circuit voltage (OCV), incrementally increasing the scan range until run-away current (>0.2 mA cm^{-2}). Na electrochemistry was explored on a Cu working electrode, Na-metal reference electrode and a Pt wire counter electrode; all electrodes were cleaned prior to use and the Cu electrode was polished with 0.3 um beta-alumina and water slurry. The cell was cycled from OCV to −1.4 V to 2 V at 100 mV s^{-1} at 50 °C with Z_{IR}

correction determined by the x-intercept of the first touch-down on the Nyquist plot.

The Al electrodes were punched from a roll of battery-grade Al-foil with 19 mm diameter hollow punch. Sodium metal counter electrodes were prepared by rolling-out a Na metal chunk into a foil, first placed within a plastic bag before rolling on a glass pane. 18 mm diameter disks of Na metal were punched from the foil. The 2032 coin-cells were fabricated in an Ar-glovebox with a Solupor PE separator and 50 μL electrolyte. At either RT or 50 °C, the cells were at OCV for 12 h before cyclic voltammetry (OCV start) from 3 V to 7 V with a scan rate of 1 mV s^{-1} on a Biologic VMP2 or VMP3e potentiostat. Following the CV, the cell was held at OCV for 1 minute before the LSV to 7 V at 1 mV s^{-1}. The CA at 7 V for 12 h commenced immediately after the LSV sweep.
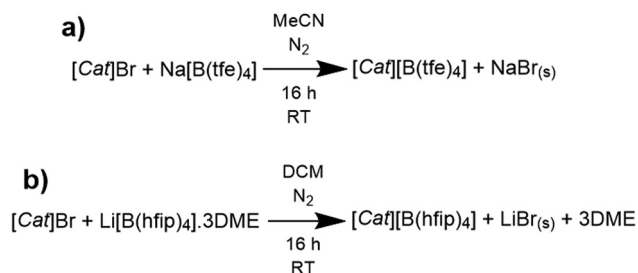
Surface characterisation

The materials were investigated by a scanning electron microscope (JEOL JSM-7001F FEG-SEM) at an accelerating voltage (HT) of 15 kV and EDS that is attached to the microscope. The samples were attached on the SEM specimen holder with supporting stubs with double-side conducting carbon tape.

X-ray photoelectron spectroscopic (XPS) analysis was performed using a Nexsa Surface Analysis System (Thermo Fisher Scientific). Analysis was undertaken with a monochromated Al Kα source at a power of 180 W (15 kV × 12 mA) and a hemispherical analyser operating in a fixed analyser transmission mode. The total pressure in the main vacuum chamber during the analysis was typically between 10^{-9} and 10^{-8} mbar. Survey spectra were acquired at a pass energy of 200 eV and a step size of 1 eV. High-resolution spectra were recorded from individual peaks at 50 eV pass energy using 0.1 eV step size, typically yielding a full width at half-maximum (FWHM) of 0.8–0.9 eV for the Ag 3d$_{5/2}$ peak and <1.0 eV for the ester peak in poly(ethylene terephthalate) (PET) during performance tests. Samples were analysed at a nominal photoelectron emission angle of 0° with respect to the surface normal. Since the actual emission angle is ill-defined in the case of rough surfaces (ranging from 0 to 90°), the sampling depth may range from 0 to approximately 10 nm. Samples were mounted in a manner excluding any electrical contact of the analysed conductive area with the instrument ground. Data processing was performed using the ThermoScientific Avantage processing software version 5.9925. Binding energies were referenced to the C 1s peak at 284.8 eV (aliphatic hydrocarbon).

Results and discussion

Synthesis of the fluoroborate ionic liquids

The synthetic procedures to yield the six ionic liquids (ILs) are shown in Scheme 1 (see Fig. 1 for structures and Table S1, ESI† for abbreviations). Both products incorporating cation **1** were found to be room-temperature ionic liquids which is typical of ILs formed by the alkoxyammonium cation;[29] the four remaining ILs are solids at room temperature. Purification of

a)

$$[Cat]Br + Na[B(tfe)_4] \xrightarrow[\substack{16\ h \\ RT}]{\substack{MeCN \\ N_2}} [Cat][B(tfe)_4] + NaBr_{(s)}$$

b)

$$[Cat]Br + Li[B(hfip)_4]\cdot 3DME \xrightarrow[\substack{16\ h \\ RT}]{\substack{DCM \\ N_2}} [Cat][B(hfip)_4] + LiBr_{(s)} + 3DME$$

Scheme 1 Generalised reaction schemes of for the metathesis of the (a) $[B(tfe)_4]^-$ and (b) $[B(hfip)_4]^-$ ILs where $[Cat]^+$ represents either $[N_{2(2O2O1)3}]^+$, $[P_{122i4}]^+$ or $[C_3mpyr]^+$. Note: for $[P_{122i4}]^+$, the tosylate $([H_3C(C_6H_4)SO_3]^-)$ salt is used instead of Br^-. MeCN is acetonitrile and DCM is dichloromethane.

the $[B(hfip)_4]^-$ ILs is possible *via* an aqueous biphasic extraction which achieves sufficient purification for the electrochemistry studied here. Unfortunately, the same procedure is not suitable for the $[B(tfe)_4]^-$ ILs due to the tendency of the product to favour the aqueous phase. Purification was therefore limited to filtration and centrifuging techniques which prohibits the complete removal of Na^+ species in the products. Inductively coupled plasma optical emission spectroscopy (ICP-OES) measurements determined residual alkali ions was present at trace quantities (<1000 ppm) for all products excluding **1a** and **3a** (Table S2, ESI†). Unfortunately, the measured concentration of Na^+ reflects the maximum solubility of Na^+ which is probably a mixture of $Na[B(tfe)_4]$ and NaBr. Both **1a** and **3a** measured a high Br^- content by ICP-OES (Table S2, ESI†) which was expected to limit electrochemical investigations. The synthesis of **1b** instead used the tosylate (*i.e.* $[CH_3(C_6H_4)SO_3]^-$) pathway instead of Br^-, however the sodium tosylate by-product was detected by NMR. The ^{1}H-NMR spectra of the purified materials synthesised are shown in Fig. S2–S7 (ESI†).

Single-crystal X-ray diffraction (SC-XRD) crystal structures of **2a**, **3a** and **3b** were obtained from crystals grown in a DCM/*n*-hexane slow diffusion crystallisation set-up, with DCM as the solvent and hexane as the anti-solvent. The vials were stored at room-temperature and crystals were collected after one week. A summary of the crystal structure data is available in Table S3 (ESI†) and the structures of **2a**, **3a** and **3b** are available in Fig. S7–S9 (ESI†). Attempts to obtain crystals of **2b** of suitable quality for SC-XRD analysis were unsuccessful. At room-temperature (RT), crystals of **2b** were found to be malleable and tacky. Notably, this is characteristic plastic behaviour and explains the poor-quality diffraction observed for these crystals.

Physical characterisation

Phase change behaviour. Differential scanning calorimetry (DSC) heating traces in Fig. 2 show all observed transitions in the first heating cycling of the six synthesised compounds between −120 °C and their melting point (T_m) (cooling traces are shown in Fig. S10, ESI†). Both **1a** and **1b** did not display a T_m, instead a glass transition (T_g) was measured for both compounds at −74 and −73 °C, respectively. The DSC traces of the first three heating and cooling cycles of all materials are shown in Fig. S11–S16 (ESI†). The low T_g of these ILs is comparable to $[N_{2(2O2O1)3}][TFSI]$, which exhibits a T_g at −68 °C.

The low entropies of fusion (ΔS_f) of **2b** and **3b** (17 and 18 J mol^{-1} K^{-1}, respectively), which are calculated from the first law of thermodynamics ($\Delta S = \Delta H/T_m$), suggest that these materials exhibit organic ionic plastic crystal (OIPC) behaviour. OIPCs typically exhibit only a small (<20 J mol^{-1} K^{-1}) ΔS_f upon melting,[45] due to their highly disordered "plastic" phases that exist prior to melting; this disorder contributes to high mobility in these solid phases.[46,47]

All materials analysed here undergo solid-state transitions prior to melting and the solid-state phases are denoted here by IV, III, II and I, where I is the highest temperature solid phase. These transitions are typically associated with the onset of translational, rotational or orientational motions of the ions, or crystallographic changes in the material.[48,49] **2b** and **3b**
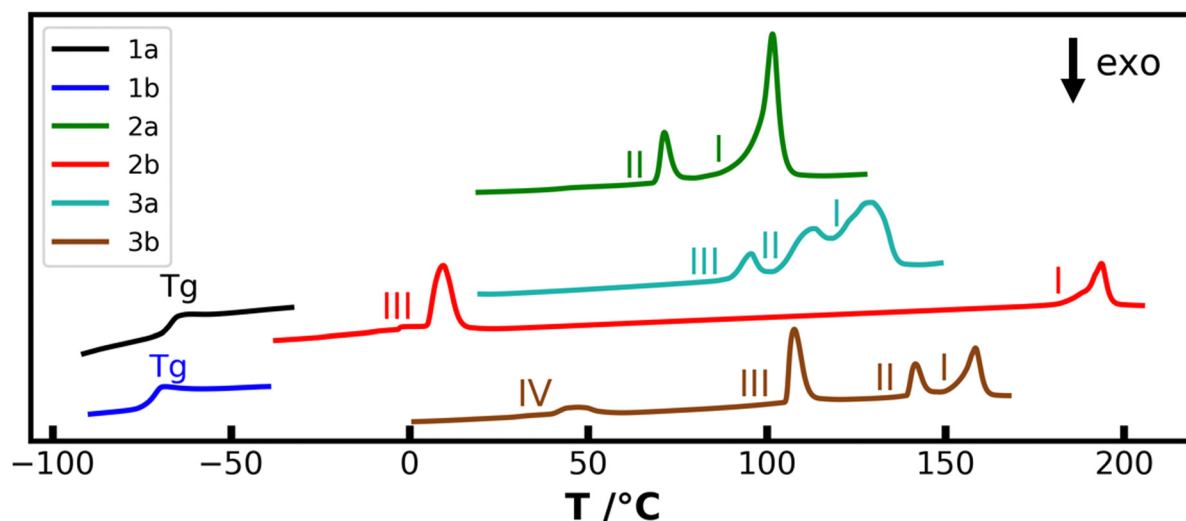

Fig. 2 Differential scanning calorimetry (DSC) traces of all synthesised compounds from −120 °C to T_m at 10 °C min^{-1}. The first heating cycle is shown for all compounds excluding **2b** where the 3rd cycle is shown to include the melt.

27722 | *Phys. Chem. Chem. Phys.*, 2023, **25**, 27718–27730

This journal is © the Owner Societies 2023

Table 1 Phase transitions for the borate ILs, extracted from the DSC thermograms. Dashed entries are for convoluted transitions which are integrated together

| | Glass transition | Solid–solid transitions | | | | | | Melt | |
| | T_g | Phase IV–III | | Phase III–II | | Phase II–I | | Phase I–melt | |
	$T_g \pm 1/°C$	$T_{ss} \pm 1/°C$	$\Delta S \pm 10\%/$ $J\ K^{-1}\ mol^{-1}$	$T_{ss} \pm 1/°C$	$\Delta S \pm 10\%/$ $J\ K^{-1}\ mol^{-1}$	$T_{ss} \pm 1/°C$	$\Delta S \pm 10\%/$ $J\ K^{-1}\ mol^{-1}$	$T_m \pm 1/°C$	$\Delta S_f \pm 10\%/$ $J\ K^{-1}\ mol^{-1}$
1a	−74								
1b	−73								
2a						70	10	100	47
2b				9	46	—	—	189	17
3a				90	5.0	113	—	128	38
3b		47	6.5	108	25	142	8.2	158	18

exhibit several solid–solid transitions prior to the melt and the calculation of ΔS (Table 1) shows both materials undergo low entropy melting transitions; these compounds therefore likely have high entropy in the solid phases. Furthermore, **2b** exhibits the disordered phase I (ΔS_{III-I} = 46 J mol^{-1} K^{-1}, ΔS_f = 17 J mol^{-1} K^{-1}) at room temperature (RT). On cooling, two exotherms are observed with a combined entropy of 46 J mol^{-1} K^{-1}, indicating the endothermic transition observed at 9 °C is likely a two-step process or a convoluted peak representing both the III–II and II–I transitions, hence the lower temperature phase is denoted III. Materials which display OIPC behaviour at RT are of strong research interest for a variety of applications which include atmospheric gas separation and solid-state electrolytes.[49–52] The broad temperature range of the phase I of **2b** (9 to 180 °C) is ideal as it provides the opportunity to utilise the unique properties of the plastic phase over a large temperature range.[48,49]

The T_m of the $[B(tfe)_4]^-$ (**a**) compounds were lower for both $[P_{122i4}]^+$ and $[C_3mpyr]^+$, when compared to their respective $[B(hfip)_4]^-$ salts (Table 1). For example, the T_m of **2a** is 100 °C whereas the T_m of **2b** is 188 °C. The difference in melting point is attributed to the additional molar mass of $[B(hfip)_4]^-$.

The first heating cycle is shown for all compounds, except **2b**, where the 3rd cycle is shown instead to include the high T_m; the material was not originally cycled to this temperature due to decomposition concerns around 200 °C. Both **3a** and **3b** displayed evidence of decomposition after their first melting transitions. The second cycle for **3a** and **3b** (Fig. S15 and S16, ESI,† respectively) was altered compared to the first with phase II to I and the melting temperature merging to a single peak which implies partial decomposition of the analysed material (as decomposition products serve as impurities which can broaden transitions and decrease transition temperatures).[53]

Thermal stability and flammability. The thermal stability of the salts was further probed by thermal gravimetric analysis (TGA); traces are shown in Fig. S17 (ESI†). The decomposition temperature (T_d) in Table 2, determined from the point of 5% mass loss, shows the upper limit of thermal stability of most of the ILs to be approximately 200 °C, however the T_d of **1a** is notably lower at 132 °C. These values of T_d's are comparable to the thermal stability of ILs with structurally similar alkyl-borate anions, which indicates that the observed limit is likely due to

the nature of the alkyl-borates.[54,55] Regardless, a T_d onset of 200 °C is adequate for most applications. More important to consider is the safety aspects of decomposition of a material, which are not necessarily reflected in T_d. Thus further small-scale experiments investigating the flammability of the novel materials are described in the following section.[9,10,56]

Ionic liquids are often described as being non-flammable, despite combustion being a complex and unpredictable process therefore materials should be judged on a case-by-case basis.[11,57] In the flammability test, a small sample is exposed to an ignition source until combustion, after which the ignition source is removed and the sample is observed for self-sustaining behaviour.[10] Still images and experimental observations from video recordings of the tests are available in the ESI† (Fig. S18–S24) with a brief discussion of experimental observations; a summary of the results are shown in Table 2. The image in Fig. 3a shows the material **1a** after 2 s of combustion with an applied ignition source, which sustained combustion for 9 s following ignition source removal (Fig. 3b); the sample was entirely consumed and left minimal residue. TGA was concordant with this observation by also recording 100% mass loss.

The suspected source of the flammability is attributed to disassociation of the anion into known highly volatile and flammable compounds $B(tfe)_3$ and $Na[tfe]$ (tfe = $-OCH_2CF_3$).[8,30] In contrast, Fig. 3c shows the combustion of **1b** which quickly extinguished upon removal of the ignition source, as shown in Fig. 3d. The self-extinguishing time following removal of the ignition source for all samples is shown in Fig. 3e. $[C_3mpyr][FSI]$ was used as an experimental benchmark; this was found to be combustible but not self-sustaining, therefore non-flammable. **1b** behaved identically to the $[C_3mpyr][FSI]$ and therefore possesses a comparably low flammability hazard profile. Overall, $[B(hfip)_4]^-$ salts all displayed safety profiles equivalent to the experimental benchmark making them highly appealing for large-scale energy storage applications.

Ionic conductivity of organic salts and ionic liquids. The following sections aim to understand the physical properties of the novel salts (limited to conductivity only for products which are solids at RT).

Solid-state conductivity measurements were made to determine the ionic mobility of the organic salts. Such physicochemical properties are crucial in electrochemical applications such

Table 2 Summary of thermal decomposition (T_d, determined at 5% mass loss), material flammability, conductivity, density, viscosity, and electrochemical window against glassy carbon (GC) of the synthesised ILs

| Compound	T_m/°C	T_d (−5%)/°C	Flammable?	σ (50 °C)/S cm^{-1}	ρ (50 °C)/g cm^{-3}	η (50 °C)/mPa s	ECW (WE: GC)/V	
							vs. Fc$^+$/Fc	*vs.* Na$^+$/Na
1a	−74[a]	132	Yes	9.4×10^{-4}	1.25	40.1	Up to 1.0	Up to 4.1
1b	−73[a]	207	No	1.6×10^{-3}	1.39	21.1	−3.1 to 2.2	0.0 to 5.3
2a	100	168	Yes	5.1×10^{-4}	—	—	—	
2b	189	210	No	3.7×10^{-6}	—	—	—	
3a	128	200	Yes	2.4×10^{-4}	—	—	—	
3b	158	185	No	1.4×10^{-4}	—	—	—	
[C$_3$mpyr][FSI]	−9	319	No	1.6×10^{-2}	1.32	20.1	−3.0 to 2.3[25]	0.1 to 5.4
[N$_{2(2O2O1)3}$] [TFSI][38,58]	−68[a]	300	—	3.5×10^{-3}	1.28	25.7	Up to 1.3	Up to 4.4
[N$_{2(2O2O1)3}$] [*closo*-CB$_{11}$H$_{12}$][29]	−47[a]	300	—	3.9×10^{-4}	1.01	269	Up to 1.7	Up to 4.7

[a] T_g observed instead of T_m.
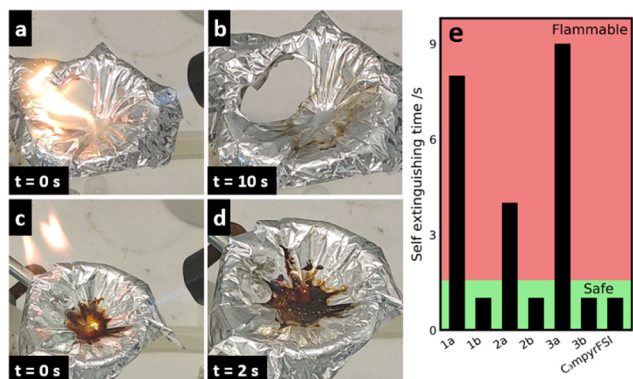
Fig. 3 Still images at key time-points of the flammability experiments for **1a** at (a) 2 s and (b) 12 s following ignition showing the sustained combustion of **1a**. Stills at (c) 5 s and (d) 7 s of **1b** show non-sustained combustion following removal of the ignition source. The (e) self-extinguishing times of all analysed samples; safe ILs are indicated by a self-extinguishing time of <2 s (shown by the green region).
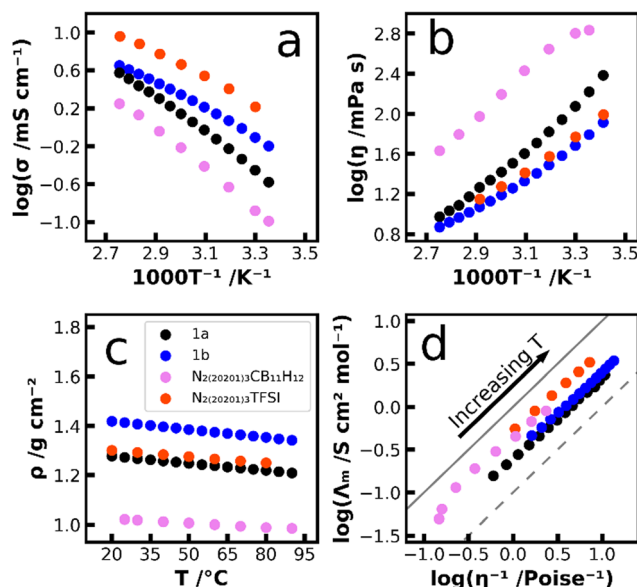

Fig. 4 (a) Conductivity, (b) viscosity, (c) density and (d) Walden analysis of the RTILs **1a** and **1b**. Data for [N$_{2(2O2O1)3}$][*closo*-CB$_{11}$H$_{12}$] and [N$_{2(2O2O1)3}$][TFSI] were obtained from literature.[29,38] The solid and dashed grey lines on the Walden plot represent the Ideal KCl and 10% ionicity lines, respectively.

as batteries in determining the transport of charged ions through the electrolyte; the results are summarised in Table 2 and plotted in Fig. S25 (ESI†) along with some benchmark data from the literature. The conductivity of the ILs **1a** and **1b** is shown in Fig. 4a. The measured values of **1a** and **1b** at 50 °C (9.4×10^{-4} and 1.6×10^{-3} S cm^{-1}, respectively, Table 2) are lower in comparison to [N$_{2(2O2O1)3}$][TFSI] (3.5×10^{-3} S cm^{-1}), due to the smaller anion volume of [TFSI]$^-$ relative to the fluoroborates. Conductivity for **1a** and **1b** was higher than [N$_{2(2O2O1)3}$][*closo*-CB$_{11}$H$_{12}$] (3.9×10^{-4} S cm^{-1}) which implies fewer charge-neutral ion aggregates which cannot contribute to bulk conductivity.

The measured conductivity of all of the solid ILs particularly **2b** (1.0×10^{-9} S cm^{-1} at 30 °C) was lower than published data for [N$_{111,1O1}$][FSI] which exhibits an impressive conductivity of 9.9×10^{-6} S cm^{-1} at 30 °C. The low conductivity for the newly designed materials is thought to be a consequence of the bulky fluoroborate anion. The steric bulk of the fluoroborate anions inherently hinders diffusion of the anion which counteracts the reduced electrostatic pairing. This is evident when comparing solid-state conductivities of [B(tfe)$_4$]$^-$ and [B(hfip)$_4$]$^-$ salts

where the smaller [B(tfe)$_4$]$^-$ anion exhibits higher conductivity with either cation.

Density and viscosity of room-temperature ionic liquids. Viscosity measurements of the synthesised ILs **1a** and **1b** are shown in Fig. 4b with comparison to [N$_{2(2O2O1)3}$][TFSI] and [N$_{2(2O2O1)3}$][*closo*-CB$_{11}$H$_{12}$],[29,59] a summary of the results is available in Table 2. The viscosity of **1b** was lower compared to the similar material [N$_{2(2O2O1)3}$][TFSI] which is surprising considering the additional anion bulk of the fluoroborates. The difference in viscosity may be related to a combination of factors however the charge-diffuse nature and high degree of fluorination are considered most influential. The viscosity of **1a** was higher than **1b** (40.1 and 21.1 mPa s, respectively at 50 °C) which is attributed to the higher degree of fluorination of [B(hfip)$_4$]$^-$. The density of the IL in Fig. 4c show **1b** measuring

27724 | *Phys. Chem. Chem. Phys.*, 2023, **25**, 27718–27730

This journal is © the Owner Societies 2023

1.44 g mL^{-3} at 25 °C, higher than **1a**, [N$_{2(2O2O1)3}$][TFSI] and [N$_{2(2O2O1)3}$][*closo*-CB$_{11}$H$_{12}$] (1.30, 1.29 and 1.02 g mL^{-3}, respectively). The high density of **1b**, particularly in relation to **1a**, is explained by the additional –CF$_3$ functionalisation of the anion; fluorination is also likely the reason behind the low viscosities of **1a** and **1b** by reducing the strength of transient intermolecular interactions. The effect of fluorination is visible *via* comparison of [B(hfip)$_4$]$^-$ to the F-free [*closo*-CB$_{11}$H$_{12}$]$^-$ anion which exhibits the highest viscosity by a significant margin (21.1 and 269 mPa s, respectively).

Ionicity of room-temperature ionic liquids. The Walden analysis provides further insight into the overall ionicity of the ILs and is shown in Fig. 4d. Although marginally lower than the comparison materials, **1a** and **1b** both lie within the 'good IL' region (considered to be the region between 10 and 100% ionicity lines), indicating both ILs possess sufficient ion dissociation for application as electrolytes.[21,23] Although **1a** and **1b** both exhibited lower ionicity than [N$_{2(2O2O1)3}$][*closo*-CB$_{11}$H$_{12}$], their viscosities were substantially lower which is a key property for electrochemical applications. The difference in ionicity relates to the stronger inter-ionic interactions which likely result from greater hydrogen bonding or dipole moments with either [B(tfe)$_4$]$^-$ and [B(hfip)$_4$]$^-$.

Vogel–Tammann–Fulcher analysis. Conductivity measurements of **1a** and **1b** were fitted to the Vogel–Tammann–Fulcher (VTF) equation (eqn (1))

$$\sigma = \sigma_0 \exp[-k_\sigma/(T - T_\sigma)] \qquad (1)$$

which describes the temperature dependence of conductivity of the RTILs. The experimental values for σ (S cm^{-1}) and T (K) were fitted with eqn (1), σ_0, k_σ (K) and T_σ being the fitting parameters. The number of charge carriers in the system is considered to be related to σ_0, k_σ is the pseudo-activation energy for ion transport and T_0 is the temperature where σ approaches zero.[30,60–62] Table S4 (ESI†) contains the fitted parameters for the ILs **1a**, **1b** and [C$_3$mpyr][FSI] all of which achieved good fits ($r^2 > 0.99$) in the temperature range studied; the plots of experimental data and fitted VTF equation are shown in Fig. S26 and S27 (ESI†). [C$_3$mpyr][FSI] was chosen as the benchmark in this instance due to the exceptional physical properties of the IL such as its low viscosity and high conductivity (5.7 mS cm^{-1} at room temperature).[63]

T_0 is often referred to as the ideal glass transition temperature and often lies 20–50 °C below experimental data, as observed for **1a** and **2b**; DSC experiments have determined the T_g to be 200 and 201 K respectively. [C$_3$mpyr][FSI] measured a higher conductivity than both **1a** and **1b** which is reflected in the σ_0 values however the difference of k_σ between **1b** and [C$_3$mpyr][FSI] was not significant, given the large standard deviation in the value for [C$_3$mpyr][FSI].

Viscosity data was also fitted to a VTF type equation (eqn (2))

$$\eta = \eta_0 \exp[k_\eta/(T - T_\eta)] \qquad (2)$$

where η_0 relates to the viscosity at infinite temperature, k_η is the pseudo activation energy for viscosity.[30] Unlike the conductivity fit, **1b** and [C$_3$mpyr][FSI] possessed similar η_0 values however **1b**

was marginally lower and indicates higher fluidity at high temperatures. Values for k_η show that **1b** exhibits the lowest pseudo activation energy, followed by [C$_3$mpyr][FSI] then **1a**; the same order was observed for k_σ. The T_η fits for **1a** and **1b**, were only 19 and 6 K below the experimentally determined T_g; this may imply that the low-temperature data is inaccurate.

Both fluoroborate ILs have shown potential for electrochemical applications, which is further investigated in the following section. The electrochemical window is initially investigated, followed by Na-cycling and cathodic passivation of Al of the best material.

Electrochemical characterisation

Electrochemical stability for **1b** was first investigated *via* a three-electrode cell against a glassy carbon (GC) working electrode at RT under argon (Ar) atmosphere. **1a** was not studied electrochemically due to the known [Br]$^-$ content. Fig. 5a shows the 5.3 V ECW of **1b** against a GC electrode. During the experiment the maximum potential for each sweep was gradually increased until runaway current is observed. The sixth and eighth cycle display the decreasing currents as the native GC surface is passivated; the mechanism for passivation is currently unknown. The ninth cycle appears to be the 2.2 V (*vs.* Fc$^+$/Fc, 5.3 V *vs.* Na$^+$/Na) oxidative limit of **1b**. This work improves upon the 5 V (*vs.* Li$^+$/Li) window of 0.5 M Li[B(hfip)$_4$]·3DME/EC : DMC (1 : 1 vol), despite the ether ammonium cation which often exhibits lower stabilities.[29,59] The oxidative stability of 2.2 V (*vs.* Fc$^+$/Fc, 5.3 V *vs.* Na$^+$/Na) for **1b** is higher than the 2.1 V limit of [P$_{111i4}$][FSI], one of the most electrochemically stable ILs known.[39] It substantially improves upon the stability of [N$_{2(2O2O1)3}$]$^+$ ILs with alternative anions such as [*closo*-CB$_{11}$H$_{12}$]$^-$ or [TFSI]$^-$ which display stabilities of 4.4 and 4.7 V (*vs.* Na$^+$/Na), respectively.[29,59] This suggests that **1b** does not oxidise easily at high oxidative potentials up to 5.3 V (*vs.* Na$^+$/Na). This makes it an excellent candidate as a
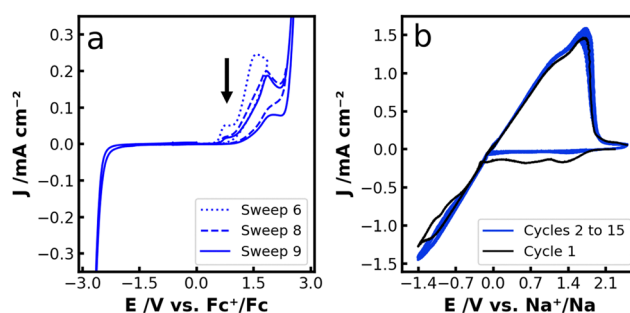

Fig. 5 Three-electrode CV traces of the (a) ECW^a of **1b**, earlier sweeps are shown with the dotted and dashed traces with the passivation indicated by the black arrow (WE: GC, CE: Pt, RE: Pt) at RT. Cell potential was referenced to a ferrocenium/ferrocene redox-couple. (b) CV trace of the Na$^+$/Na redox with 50 mol% Na[FSI] in **1b** (WE: Cu, CE: Pt, RE: Na) in the potential range of −1.4 to 2.0 V at 100 mV s^{-1} at 50 °C. All 15 cycles are shown where black is the first cycle and subsequent cycles in blue. ^{a}oxidative and reductive stability were measured separately and plotted together.

This journal is © the Owner Societies 2023

Phys. Chem. Chem. Phys., 2023, **25**, 27718–27730 | **27725**

battery electrolyte with high-voltage cathodes which function at high operating voltages (*i.e.* > 4.0 V *vs.* Na$^+$/Na).[64]

To confirm the applicability of **1b** in a Na electrochemical system, a three-electrode cell with a copper working electrode was prepared. The cyclic voltammetry trace with Na[FSI] : **1b** (at 1 : 1 molar ratio) is shown in Fig. 5b. In the first cycle (black) a coulombic efficiency of 72% and a maximum deposition current density (J_{max}) of 1.4 mA cm^{-2} at -1.4 V *vs.* Na$^+$/Na was achieved. The overpotential for Na deposition onset was measured at -80 mV *vs.* Na$^+$/Na which implied the energy barrier for deposition is low. The J_{max} of Na[FSI]:**1b** was lower than the similar Na[FSI]:[N$_{2(2O2O1)3}$][FSI] system (J_{max} = 12 mA cm^{-2}) and is believed to result from the lower molar Na$^+$ concentration (1.2 M) of Na[FSI]:**1b** which is a consequence of the bulky anion of **1b**.[59] The Na[FSI]:**1b** electrolyte outperforms other alkoxyammonium RTILs such as [N$_{2(2O2O1)3}$][TFSI] with 2.0 mol kg^{-1} Na[TFSI] which measured a J_{max} of 0.18 mA cm^{-2} (10 mV s^{-1}, 50 °C).[60] The cell cycling behaviour over 15 cycles with Na[FSI]:**1b** shows consistent deposition and stripping currents which implies stable electrochemical cycling of Na. In the first cycle (black trace), solid–electrolyte interface formation on the native Cu surface can be seen by the elevated current from ∼1.5 V to the potential of Na^0 deposition. Currents for Na^0 deposition were very stable across the 15 cycles where two convoluted peaks were observed which suggests two or more oxidative mechanisms occurring. Elucidation of these processes was not attempted as in-depth studies outside of the scope of this work would be required.

High-voltage aluminium passivation. Aluminium as the current-collector material is an essential component of battery electrodes, therefore sufficient oxidative stability and/or passivation is required. The voltammetry sweeps in Fig. 6a are of two coin-cells (WE: Al, CE/RE: Na) with either **1b** or Na[FSI]:**1b**. A maximum potential of 7 V (*vs.* Na$^+$/Na) was applied to these coin-cells at 50 °C. The J_{max} of the neat IL measured 14.6 µA cm^{-2} which occurred at 7 V in the first cycle, was significantly higher than the J_{max} of Na[FSI]:**1b** (0.6 µA cm^{-2}). Each subsequent cycle for both electrolytes saw a decrease in current which is characteristic of surface passivation.[65–67] Immediately following the sixth sweep to 7 V, the cell was held at 7 V for 12 h (Fig. 6b) during which time the currents

decrease, this being typical electrochemical behaviour for surface passivation.[32,34,68] The passivation of Al by **1b** or Na[FSI]:**1b** is more effective than was observed with [C$_3$mpyr][FSI],[68] which is indicated by the lower currents and higher potentials achieved here. Thus the IL electrolytes in this study greatly improve the upper potential limit compared to 0.5 M DME electrolytes with Na[B(tfe)$_4$] or Na[B(hfip)$_4$] (4.5 V *vs.* Na$^+$/Na) which is attributed to the poor oxidative stability of the DME solvent.

Notably, the electrochemical data implies the passivation behaviour was substantially improved with the addition of Na[FSI] seen by the lower currents; the exact role of [FSI]$^-$ is further understood in the surface analysis in the following section. The Na[FSI]:**1b** electrolyte displayed an impressively low current of 0.037 µA cm^{-2} after 12 h of polarisation at 7 V this being representative of the leakage current of the Al current-collector. Compared to Na[FSI]:**1b**, neat **1b** at 50 °C was less stable and exhibited a temporary increase in current at 2 h (from 1.5 to 1.6 µA cm^{-2}) in the CA experiment (Fig. 6b), which is suspected to be caused by Na$^+$ ions from the CE reaction becoming involved in the WE process which compromises the passivation layer. Dissolution is often enhanced with increasing temperatures which may explain the worse passivation at 50 °C with neat **1b**.

The electrochemical data for the anodisation of Al at the very high potential of 7 V (*vs.* Na$^+$/Na) is promising for all systems however each system showed a varying degree of passivation effectiveness. To further understand the passivation behaviour between electrolytes, the foils were recovered after the electrochemisty shown and analysed to investigate the morphology and chemical composition of the anodised foils.

Surface analysis of passivated aluminium. The recovered foils were analysed post-mortem by scanning electron microscopy (SEM) with elemental mapping by energy dispersive X-ray spectroscopy (EDX). The surfaces of the anodised foils are distinctly modified when compared to the pristine Al foil in Fig. 7a. The foil anodised with Na[FSI]:**1b** is shown in Fig. 7b. The deposition on the foil surface is notably consistent and smooth. A cross-section of the foil anodised with Na[FSI]:**1b** is shown in Fig. 7c which highlights the smooth morphology of the deposition. The foil anodised with neat **1b** at 50 °C (Fig. 7d) displayed uneven passivation, with a rough surface across the electrode. Anodisation with neat **1b** at RT (Fig. 7e) does not produce the same rough morphology as the 50 °C foil, instead the surface is consistent with prior reports of [B(hfip)$_4$]$^-$ passivation of Al in organic electrolytes.[32,34] The cross-section of the RT anodisation (Fig. 7f) shows a smooth surface morphology, although notably rougher than the foil anodised with Na[FSI]:**1b**. It appears the combination of Na[FSI] and **1b** is synergistic in passivating Al-foil at high potentials, in a way which cannot be achieved with [FSI]$^-$ alone. An additional Al‖Na cell with neat [C$_3$mpyr][FSI] was prepared, the data is shown in Fig. S29 (ESI†). As expected, with the conventional IL, oxidative corrosion was observed as shown by the increasing and unstable currents measured, particularly in the CA section where current was unstable in the final 3 hours (ranging between 25 and 35 µA cm^{-2}).
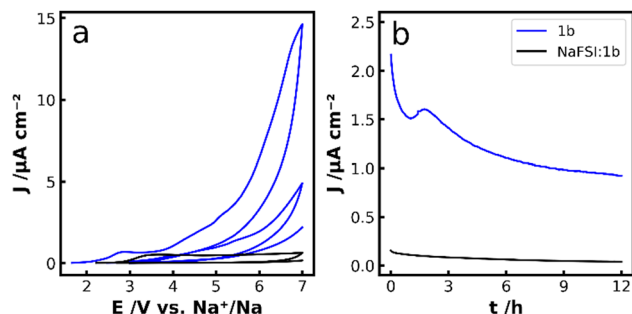

Fig. 6 The first, third and sixth voltammetry sweeps (currents decreasing with cycles) of **1b** and Na[FSI]:**1b** electrolytes in an Al‖Na coin-cell (WE: Al, RE/CE: Na) and (b) CA following the sixth voltammetry sweep at 50 °C.

27726 | *Phys. Chem. Chem. Phys.*, 2023, **25**, 27718–27730
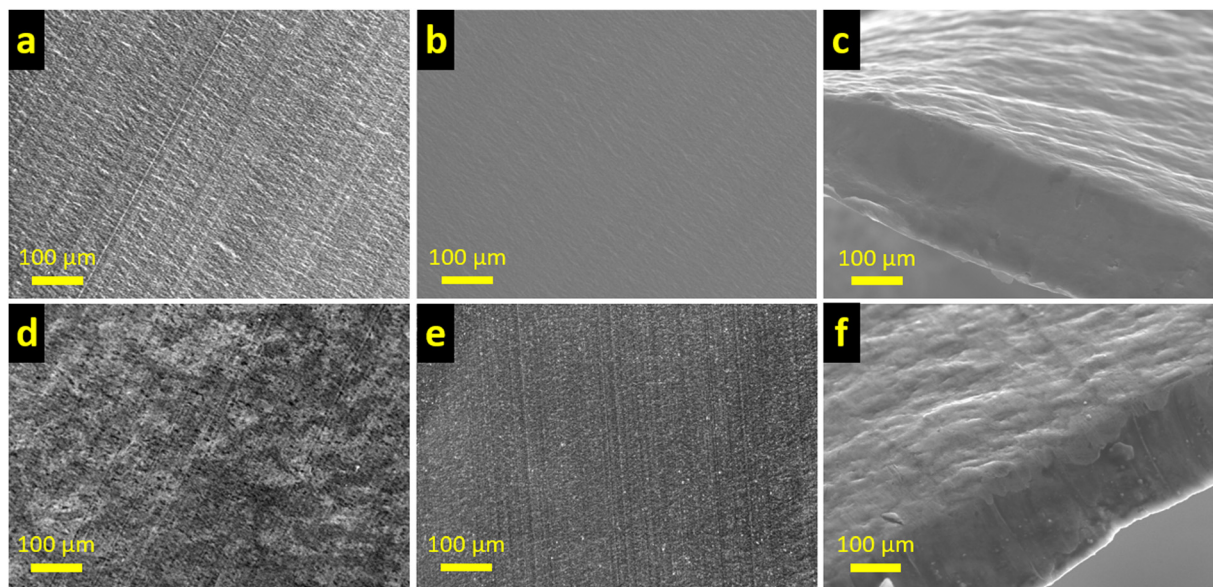
This journal is © the Owner Societies 2023

Fig. 7 SEM micrographs of (a) pristine Al current-collector foil (top-down), (b) Al-foil anodised with Na[FSI]:**1b** (top-down) and (c) cross-section of the same foil to show surface smoothness. SEM micrographs of anodised foils with neat **1b** at (d) 50 °C (top-down) and (e) RT (top-down), and the (f) cross-section of the RT anodisation to show surface roughness.

The results and discussion of the EDX data can be found in the ESI† below Table S5. The EDX data (Fig. S30–S33, ESI†) shows Na[FSI]:**1b** at 50 °C exhibits a smaller amount of electrolyte decomposition than **1b**, measuring the highest abundance of Al (87.4 and 75.9 atomic%, respectively).

The X-ray photoelectron spectroscopy (XPS) analysis of Al 2p environments on the anodised foils (Fig. 8a) show significant alteration of all surfaces when compared to the pristine Al. The surface of the pristine Al foil was as expected, with the bulk Al^0 and overlying Al_2O_3 signals at 73 and 74 eV, respectively.[68,69] Surprisingly the sample produced from **1b** at RT showed no Al 2p environment which implies an Al-free passivation layer, which is thicker than the penetration depth ($\sim$10 nm) of XPS. Al 2p was detected for **1b** at 50 °C although the weak Al^0 response implies a thickening of the passivation layer which is weighted heavily towards inorganic Al species (76–74 eV).[68,69] The Al 2p in the Na[FSI]:**1b** sample was also heavily weighted towards inorganic Al rather than Al^0 which suggests thickening of the passivation layer with additional inorganic Al compounds such as AlF_3 (76 eV) and $AlFO_2$ (75 eV).[69] Neat **1b** at 50 °C also fluorinated the native Al_2O_3 layer however AlF_3 was in lower abundance and an outcome of the inferior passivation.

The S 2p spectra are shown in Fig. S34 (ESI†) where Na[FSI]:**1b**, the only S-containing system, produced a S 2p response at 170.5 eV (FO_2S–) which is representative of the $[FSI]^-$ and/or decomposition products;[70] Na[FSI] is assumed to be removed by washing with DMC. In organic systems, $[FSI]^-$ is well-known to corrode Al foil at potentials greater than 4.3 V *vs.* Na^+/Na, which involves the formation of $Al[FSI]_3$ and/or $[FSI]^-$ decomposition products on the Al surface. $Al[FSI]_3$ exhibits high solubility in organic solvents and therefore dissolves into the electrolyte to reveal underlying Al_2O_3 or Al^0 which is continually attacked by $[FSI]^-$.[71] Fig. 8b shows the Na 1s
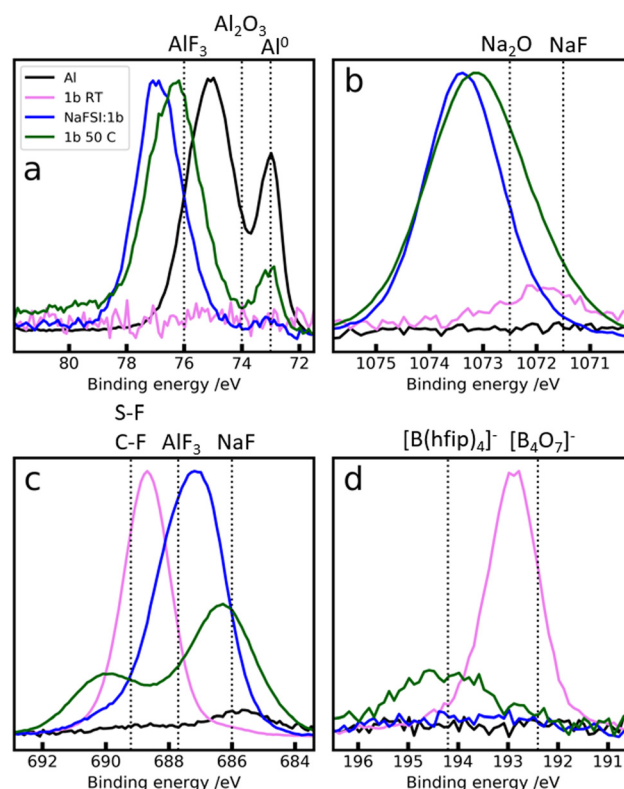

Fig. 8 X-ray photoelectron spectroscopy of the (a) Al 2p, (b) Na 1s, (c) F 1s, and (d) B 1s chemical environments detected on the Al foil surface. Important chemical species are indicated above each figure. Data for all samples is normalised and low abundance regions (*i.e.* noisy) are reduced until noise is comparable to other samples.

environments and confirms the presence of NaF (1071.5 eV) on the surface after anodisation with Na[FSI]:**1b**; higher binding

energy species were detected but their identity could not be determined and are likely complex products of electrolyte decomposition.

The dominating signals in the F 1s spectra are shown in Fig. 8c, with the **1b** at RT sample producing AlF_3 (687.7 eV) whereas for the Na[FSI]:**1b** sample, NaF and [FSI]$^-$ were the major species present.[14,32,34] The $-CF_3$ moiety detected for **1b** at 50 °C is attributed to residual electrolyte in the porous Al surface which can be seen in the SEM micrograph in Fig. S35 (ESI†). The figure is accompanied by a short discussion regarding the inferior passivation of **1b** at 50 °C. The C 1s spectra in Fig. S36 (ESI†) detected abundant $-CF_3$ for **1b** at 50 °C from the residual electrolyte. Ethereal C was also detected the surface for all anodised samples which is probably from cation decomposition products. The residual electrolyte from **1b** at 50 °C can also be observed in the nitrogen (N) 1s spectra in Fig. S37 (ESI†) at 401.6 eV which corresponds to an alkyl ammonium environment.[72] The same environment was observed for Na[FSI]:**1b** additional to the $N-SO_2$ environment (399.8 eV) which confirms the presence of Al[FSI]$_3$, or [FSI]$^-$ decomposition products.[14] The B 1s spectra in Fig. 8d shows B was a significant component only for **1b** at RT, all other samples detected negligible B. The B 1s environment detected is attributed to [B$_4$O$_7$]$^-$ and confirms its role in passivation of the Al foil. The O 1s spectra in Fig. S38 (ESI†) supports the presence of tetraborate ([B$_4$O$_7$]$^-$) (192.4 eV) after anodisation with **1b** at RT.[73]

Conclusions

This work reports novel borate ionic liquids and studies of their thermal, physical, and electrochemical properties for a broad scope of applications. All ILs prepared with [B(hfip)$_4$]$^-$ show intriguing thermal properties such as the plastic and liquid behaviour. The best material uncovered was [N$_{2(2O2O1)3}$][B(h-fip)$_4$] (**1b**), found to be a room-temperature ionic liquid which exhibits a 5.3 V electrochemical window and passivation of Al shown up to 7 V (*vs.* Na$^+$/Na). Electrochemical cycling of Na was shown with an electrolyte of an equimolar mixture of Na[FSI] and **1b** where high stability was observed over 15 cycles. Additional to the electrochemical properties, **1b** was found to exhibit good ionicity and non-flammability. The properties discovered in this work show **1b** to be a promising material for high-voltage electrochemical applications.

Conflicts of interest

There are no conflicts to declare.

Acknowledgements

References

1 L. Wong, Crews battle Tesla battery fire at Moorabool, near Geelong – ABC News, https://www.abc.net.au/news/2021-07-30/tesla-battery-fire-moorabool-geelong/100337488, (accessed 10 December 2022).

2 J. Sun, J. Li, T. Zhou, K. Yang, S. Wei, N. Tang, N. Dang, H. Li, X. Qiu and L. Chen, *Nano Energy*, 2016, **27**, 313–319.

3 F. Larsson, P. Andersson, P. Blomqvist and B. E. Mellander, *Sci. Rep.*, 2017, **7**, 1–13.

4 M. Li, J. Lu, Z. Chen and K. Amine, *Adv. Mater.*, 2018, **30**, 1800561.

5 Q. Wang, B. Mao, S. I. Stoliarov and J. Sun, *Prog. Energy Combust. Sci.*, 2019, **73**, 95–131.

6 Q. Wang, P. Ping, X. Zhao, G. Chu, J. Sun and C. Chen, *J. Power Sources*, 2012, **208**, 210–224.

7 P. Barnes, K. Smith, R. Parrish, C. Jones, P. Skinner, E. Storch, Q. White, C. Deng, D. Karsann, M. L. Lau, J. J. Dumais, E. J. Dufek and H. Xiong, *J. Power Sources*, 2020, **447**, 227370.

8 K. Tasaki, K. Kanda, S. Nakamura and M. Ue, *J. Electrochem. Soc.*, 2003, **150**, A1628.

9 H. Sun, G. Zhu, X. Xu, M. Liao, Y. Y. Li, M. Angell, M. Gu, Y. Zhu, W. H. Hung, J. Li, Y. Kuang, Y. Meng, M. C. Lin, H. Peng and H. Dai, *Nat. Commun.*, 2019, **10**, 1–11.

10 C. Arbizzani, G. Gabrielli and M. Mastragostino, *J. Power Sources*, 2011, **196**, 4801–4805.

11 D. M. Fox, J. W. Gilman, A. B. Morgan, J. R. Shields, P. H. Maupin, R. E. Lyon, H. C. De Long and P. C. Trulove, *Ind. Eng. Chem. Res.*, 2008, **47**, 6327–6332.

12 Y. Cao and T. Mu, *Ind. Eng. Chem. Res.*, 2014, **53**, 8651–8664.

13 M. Armand, F. Endres, D. R. MacFarlane, H. Ohno and B. Scrosati, *Nat. Mater.*, 2009, **8**, 621–629.

14 J. Sun, L. A. O'Dell, M. Armand, P. C. Howlett and M. Forsyth, *ACS Energy Lett.*, 2021, **6**, 2481–2490.

15 S. Aminah, M. Noor, P. C. Howlett, D. R. Macfarlane and M. Forsyth, *Electrochim. Acta*, 2013, **114**, 766–771.

16 S. Brutti, E. Simonetti, M. De Francesco, A. Sarra, A. Paolone, O. Palumbo, S. Fantini, R. Lin, A. Falgayrat, H. Choi, M. Kuenzel, S. Passerini and G. B. Appetecchi, *J. Power Sources*, 2020, **479**, 228791.

17 M. Hasanpoor, D. Saurel, R. C. Barreno, K. Fraysse, M. Echeverría, M. Jáuregui, F. Bonilla, G. W. Greene, R. Kerr, M. Forsyth and P. C. Howlett, *ACS Appl. Mater. Interfaces*, 2022, **14**, 13196–13205.

18 J. Sun, D. Rakov, J. Wang, Y. Hora, M. Laghaei, N. Byrne, X. Wang, P. C. Howlett and M. Forsyth, *ChemElectroChem*, 2022, **9**, e202200382.

19 F. Makhlooghiazad, L. A. O'Dell, L. Porcarelli, C. Forsyth, N. Quazi, M. Asadi, O. Hutt, D. Mecerreyes, M. Forsyth and J. M. Pringle, *Nat. Mater.*, 2022, **21**, 228–236.

27728 | *Phys. Chem. Chem. Phys.*, 2023, **25**, 27718–27730

This journal is © the Owner Societies 2023

20 N. V. Plechkova and K. R. Seddon, *Chem. Soc. Rev.*, 2007, **37**, 123–150.

21 W. Xu and C. A. Angell, *Science*, 2003, **302**, 422–425.

22 M. Yoshizawa, W. Xu and C. A. Angell, *J. Am. Chem. Soc.*, 2003, **125**, 15411–15419.

23 W. Xu, E. I. Cooper and C. A. Angell, *J. Phys. Chem. B*, 2003, **107**, 6170–6178.

24 J. Golding, N. Hamid, D. R. MacFarlane, M. Forsyth, C. Forsyth, C. Collins and J. Huang, *Chem. Mater.*, 2001, **13**, 558–564.

25 H. Matsumoto, H. Sakaebe, K. Tatsumi, M. Kikuta, E. Ishiko and M. Kono, *J. Power Sources*, 2006, **160**, 1308–1313.

26 M. Egashira, T. Asai, N. Yoshimoto and M. Morita, *Electrochim. Acta*, 2011, **58**, 95–98.

27 J. L. Allen, D. W. McOwen, S. A. Delp, E. T. Fox, J. S. Dickmann, S. D. Han, Z. Bin Zhou, T. R. Jow and W. A. Henderson, *J. Power Sources*, 2013, **237**, 104–111.

28 J. Chen, Z. Huang, C. Wang, S. Porter, B. Wang, W. Lie and H. K. Liu, *Chem. Commun.*, 2015, **51**, 9809–9812.

29 M. Kar, O. Tutusaus, D. R. MacFarlane and R. Mohtadi, *Energy Environ. Sci.*, 2019, **12**, 566–571.

30 S. Bulut, P. Klose and I. Krossing, *Dalton Trans.*, 2011, **40**, 8114.

31 A. B. A. Rupp, P. Klose, H. Scherer and I. Krossing, *ChemPhysChem*, 2014, **15**, 3729–3731.

32 B. Roy, P. Cherepanov, C. Nguyen, C. Forsyth, U. Pal, T. C. Mendes, P. Howlett, M. Forsyth, D. MacFarlane and M. Kar, *Adv. Energy Mater.*, 2021, **11**, 2101422.

33 D. M. C. Ould, S. Menkin, H. E. Smith, V. Riesgo-Gonzalez, E. Jónsson, C. A. O'Keefe, F. Coowar, J. Barker, A. D. Bond, C. P. Grey and D. S. Wright, *Angew. Chem.*, 2022, **134**, e202202133.

34 D. T. Duncan, B. Roy, S. L. Piper, C. Nguyen, P. Howlett, M. Forsyth, D. R. MacFarlane, J. Sun and M. Kar, *J. Phys. Chem. C*, 2022, **126**, 18918–18930.

35 R. Gond, W. van Ekeren, R. Mogensen, A. J. Naylor and R. Younesi, *Mater. Horiz.*, 2021, **8**, 2913.

36 Y. Wang, R. Jiang, Y. Liu, H. Zheng, W. Fang, X. Liang, Y. Sun, R. Zhou and H. Xiang, *ACS Appl. Energy Mater.*, 2021, **4**, 7376–7384.

37 C. S. M. Kang, O. E. Hutt and J. M. Pringle, *ChemPhysChem*, 2022, **23**, e202200115.

38 M. Hilder, M. Gras, C. R. Pope, M. Kar, D. R. MacFarlane, M. Forsyth and L. A. O'Dell, *Phys. Chem. Chem. Phys.*, 2017, **19**, 17461–17468.

39 G. M. A. Girard, M. Hilder, H. Zhu, D. Nucciarone, K. Whitbread, S. Zavorine, M. Moser, M. Forsyth, D. R. Macfarlane and P. C. Howlett, *Phys. Chem. Chem. Phys.*, 2015, **17**, 8706–8713.

40 H. Yoon, H. Zhu, A. Hervault, M. Armand, D. R. MacFarlane and M. Forsyth, *Phys. Chem. Chem. Phys.*, 2014, **16**, 12350–12355.

41 CrysAlisPRO, *Oxford Diffr./Agilent Technol. UK Ltd.*

42 G. M. Sheldrick, *Acta Crystallogr., Sect. C: Struct. Chem.*, 2015, **71**, 3–8.

43 G. M. Sheldrick, *Acta Crystallogr., Sect. A: Found. Crystallogr.*, 2015, **71**, 3–8.

44 O. V. Dolomanov, L. J. Bourhis, R. J. Gildea, J. A. K. Howard and H. Puschmann, *J. Appl. Crystallogr.*, 2009, **42**, 339–341.

45 J. Timmermans, *J. Phys. Chem. Solids*, 1961, **18**, 1–8.

46 U. A. Rana, M. Forsyth, D. R. Macfarlane and J. M. Pringle, *Electrochim. Acta*, 2012, **84**, 213–222.

47 J. M. Pringle, *Phys. Chem. Chem. Phys.*, 2013, **15**, 1339–1351.

48 H. Zhu, D. R. MacFarlane, J. M. Pringle and M. Forsyth, *Trends Chem.*, 2019, **1**, 126–140.

49 D. R. MacFarlane, M. Forsyth, P. C. Howlett, M. Kar, S. Passerini, J. M. Pringle, H. Ohno, M. Watanabe, F. Yan, W. Zheng, S. Zhang and J. Zhang, *Nat. Rev. Mater.*, 2016, **1**, 15005.

50 N. Sirigiri, F. Chen, C. M. Forsyth, R. Yunis, L. O'Dell, J. M. Pringle and M. Forsyth, *Mater. Today Phys.*, 2022, **22**, 100603.

51 A. Basile, M. Hilder, F. Makhlooghiazad, C. Pozo-Gonzalo, D. R. MacFarlane, P. C. Howlett and M. Forsyth, *Adv. Energy Mater.*, 2018, **8**, 1703491.

52 R. Yunis, D. Al-Masri, A. F. Hollenkamp, C. M. Doherty, H. Zhu and J. M. Pringle, *J. Electrochem. Soc.*, 2020, **167**, 070529.

53 M. Kerner, N. Plylahan, J. Scheers and P. Johansson, *RSC Adv.*, 2016, **6**, 23327–23334.

54 F. U. Shah, O. I. Gnezdilov and A. Filippov, *Phys. Chem. Chem. Phys.*, 2017, **19**, 16721–16730.

55 M. Taher, F. U. Shah, A. Filippov, P. De Baets, S. Glavatskih and O. N. Antzutkin, *RSC Adv.*, 2014, **4**, 30617–30623.

56 N. Wongittharom, T. C. Lee, C. H. Wang, Y. C. Wang and J. K. Chang, *J. Mater. Chem. A*, 2014, **2**, 5655–5661.

57 M. Smiglak, W. M. Reichert, J. D. Holbrey, J. S. Wilkes, L. Sun, J. S. Thrasher, K. Kirichenko, S. Singh, A. R. Katritzky and R. D. Rogers, *Chem. Commun.*, 2006, 2554.

58 M. Kar, B. Winther-Jensen, M. Armand, T. J. Simons, O. Winther-Jensen, M. Forsyth and D. R. MacFarlane, *Electrochim. Acta*, 2016, **188**, 461–471.

59 M. Hilder, P. C. Howlett, D. Saurel, E. Gonzalo, A. Basile, M. Armand, T. Rojo, M. Kar, D. R. MacFarlane and M. Forsyth, *Electrochim. Acta*, 2018, **268**, 94–100.

60 C. R. Pope, M. Kar, D. R. MacFarlane, M. Armand, M. Forsyth and L. A. O'Dell, *ChemPhysChem*, 2016, **17**, 3187–3195.

61 D. Morales, L. Gomes Chagas, D. Paterno, S. Greenbaum, S. Passerini and S. Suarez, *Electrochim. Acta*, 2021, **377**, 138062.

62 K. Matsumoto, Y. Okamoto, T. Nohira and R. Hagiwara, *J. Phys. Chem. C*, 2015, **119**, 7648–7655.

63 S. A. M. Noor, N. C. Su, L. T. Khoon, N. S. Mohamed, A. Ahmad, M. Z. A. Yahya, H. Zhu, M. Forsyth and D. R. MacFarlane, *Electrochim. Acta*, 2017, **247**, 983–993.

64 H. Gao, I. D. Seymour, S. Xin, L. Xue, G. Henkelman and J. B. Goodenough, *J. Am. Chem. Soc.*, 2018, **140**, 18192–18199.

65 S. T. Myung, Y. Hitoshi and Y. K. Sun, *J. Mater. Chem.*, 2011, **21**, 9891–9911.

66 E. Cho, J. Mun, O. B. Chae, O. M. Kwon, H.-T. Kim, J. H. Ryu, Y. G. Kim and S. M. Oh, *Electrochem. Commun.*, 2012, **22**, 1–3.

67 Z. Hou, X. Zhang, H. Ao, M. Liu, Y. Zhu and Y. Qian, *Mater. Today Energy*, 2019, **14**, 100337.

This journal is © the Owner Societies 2023

Phys. Chem. Chem. Phys., 2023, **25**, 27718–27730 | **27729**

68 S. Theivaprakasam, G. Girard, P. Howlett, M. Forsyth, S. Mitra and D. MacFarlane, *npj Mater. Degrad.*, 2018, **2**, 13.

69 R. Ramos, G. Cunge, B. Pelissier and O. Joubert, *Plasma Sources Sci. Technol.*, 2007, **16**, 711.

70 A. Lahiri, M. Olschewski, R. Gustus, N. Borisenko and F. Endres, *Phys. Chem. Chem. Phys.*, 2016, **18**, 14782–14786.

71 L. Qiao, U. Oteo, M. Martinez-Ibañez, A. Santiago, R. Cid, E. Sanchez-Diez, E. Lobato, L. Meabe, M. Armand and H. Zhang, *Nat. Mater.*, 2022, **21**, 455–462.

72 Y. Nakayama, T. Takahagi, F. Soeda, A. Ishitani, M. Shimomura and T. Kunitake, *J. Colloid Interface Sci.*, 1988, **122**, 464–474.

73 A. Y. Kuznetsov, A. V. Kruzhalov, I. N. Ogorodnikov, A. B. Sobolev and L. I. Isaenko, *Phys. Solid State*, 1999, **41**, 48–50.